ELSEVIER

Magnetic Resonance Imaging 19 (2001) 669–676

MAGNETIC RESONANCE IMAGING

Phase contrast MRI with improved temporal resolution by view sharing: k-space related velocity mapping properties

Michael Markl*, Jürgen Hennig

University of Freiburg, Department of Radiology, Section of Medical Physics, Freiburg, Germany

Received 22 February 2001; accepted 8 April 2001

Abstract

Phase contrast techniques in combination with k-space segmented CINE imaging are widely used for the quantitative assessment of blood flow or tissue motion. The temporal resolution of the corresponding pulse sequences plays an important role concerning the potential of the method to fully detect time resolved flow or motion patterns. A further improvement of temporal or spatial resolution in phase contrast CINE MRI can be achieved by the application of view sharing. Based on simulations with point-spread-functions resulting from different cyclic flow or motion patterns an analysis of view sharing techniques in combination with phase contrast MRI is presented. Velocity mapping properties and the role of different k-space regions concerning the resulting values in the phase images and thus encoded velocities were investigated. It could be shown that the velocity induced phase shifts in phase contrast techniques are mainly encoded in the central sections of k-space which makes view sharing also suitable for velocity mapping. As a result the use of appropriate sampling and data acquisition schemes permits the assessment of flow or motion patterns with significantly improved temporal resolution without loss of functional information. In addition phantom measurements with an oscillation phantom were performed in order to validate the simulation results and to demonstrate the potential of view sharing techniques to accelerate phase contrast imaging and improve the detection of the underlying flow or motion dynamics.

Keywords: Phase contrast; CINE imaging; Velocity mapping; Flow quantification; Motion quantification

1. Introduction

Phase contrast techniques are widely used for the quantitative assessment of blood flow characteristics or tissue motion in a number of applications [1–7]. Image acquisition is usually based on cardiac gated k-space segmented CINE techniques, which are modified by additional encoding gradients in order to assess time resolved one- or multi-dimensional pixel-wise velocity vector fields [8–20]. The temporal resolution of the corresponding pulse sequences is an important parameter, which determines the potential of the method to fully resolve the flow or motion dynamics as well as to assess peak velocities.

Spatial and temporal resolution of the phase contrast CINE images can be further increased by the use of view sharing techniques for data acquisitions. Several applications of this method have already been proposed which are based on different sampling strategies while usually central parts of k-space are updated more frequently compared to outer regions of the raw data matrix [13,21–27]. For CINE MRI these methods exploit the high degree of inter-frame correlation that exists between time-resolved images.

Here we present an analysis of the use of view sharing techniques for the improvement of temporal and/or spatial resolution. Simulations on the basis of point spread functions with different velocity profiles were used to analyze the velocity mapping properties and the role of different k-space regions concerning the resulting values in the phase images and thus the encoded velocities. It could be shown that the velocity induced phase shift in phase contrast techniques is mainly encoded in the central section of k-space which makes view sharing also suitable for velocity mapping.

In addition phantom measurements with an oscillation phantom were performed in order to validate the simulation results and to demonstrate the potential of view sharing techniques to accelerate phase contrast imaging and to improve the detection of the underlying flow or motion dynamics.

* Corresponding author. Tel.: +49-761-270-5182; fax: +49-761-270-3831.

E-mail address: marklmic@ukl.uni-freiburg.de (M. Markl).

0730-725X/01/$ – see front matter
PII: S0730-725X(01)00386-1

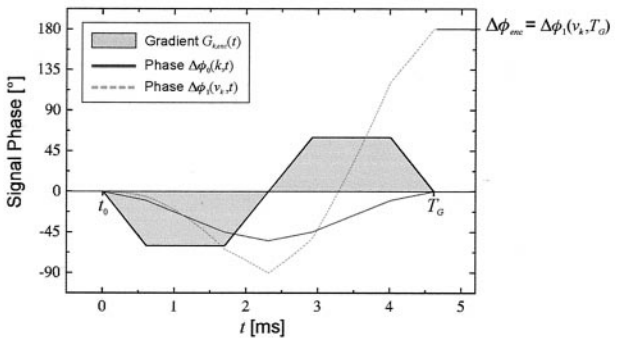

Fig. 1. Evolution of zero and first order signal phase for a bipolar velocity encoding gradient (v_{enc} = 20 cm/s). Calculations were performed for a velocity of v_k = 20 cm/s.

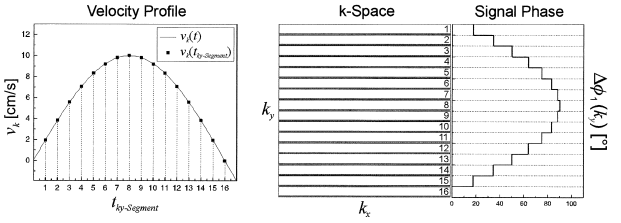

Fig. 2. Velocity induced signal phase $\Delta\phi_1(k_y, v_k(\vec{r}_0))$ as a function of the k-space position k_y for a simulated velocity profile $v_k(t)$ over a single CINE-time frame using interleaved and gated data acquisition with 16 k-space segments. The underlying velocities can be assumed constant at times $t_{ky,Segment}$ of encoding with a bipolar gradient for every single k-space line. The corresponding data points (■) determine the respective velocity and thus signal phase. Due to the repetitive k-space segmented data acquisition and corresponding sorting of the data into several k-space in an interleaved manner segments the velocity induced signal phase can be considered as a step function along the phase encoding direction (k_y).

2. Theory

2.1. Velocity encoding

First order velocity encoding is performed by the use of bipolar gradients. Moving spins will experience a linear velocity dependent phase change, which is proportional to the amplitude and duration of the gradient. Assuming constant velocities during the switching of the bipolar gradient, i.e. neglecting all higher order terms, zero and first order phase shifts introduced by a bipolar gradient in k-direction ($k = x, y, z$, are chosen as Cartesian coordinates, without loss of generality) with ramp time t_{ramp}, plateau time t_P and gradient strength G_k are given by

$$\begin{aligned}\Delta\phi_0(\vec{r}_0) &= 0\\ \Delta\phi_1(v_k(\vec{r}_0)) &= -\gamma G_k(2t_{ramp}^2 + 3t_{ramp}t_P + t_P^2)v_k(\vec{r}_0)\end{aligned} \quad (1)$$

Depending on the spatial orientation k of the bipolar encoding gradient only velocities $v_k(\vec{r}_0)$ in the corresponding direction (k) contribute to the spatially dependent phase of the MR-signal and are thus directly related to the induced first order phase shift $\Delta\phi_{enc} = \Delta\phi_1 \sim v_k(\vec{r}_0)$ (Fig. 1).

2.2. Simulations

Local signal components $S_{xy}(k_x, k_y)$ measured in an MR experiment can be written as a product of the ideal MR signal $S_{0,xy}(k_x, k_y)$ and a spatially dependent transfer function $H_{xy}(k_x, k_y)$, which describes the locally different influences on the ideal MR signal.

$$S_{xy}(k_x, k_y) = S_{0,xy}(k_x, k_y)\, H_{xy}(k_x, k_y) \quad (2)$$

If the signal properties and from that the transfer functions are known local point-spread-functions (*PSF*) can be calculated and used for simulation and estimation of complex MR intensities in object space for a given object [28,29]. The expected complex MR-image $\rho(x, y)$ can then be calculated by convolution of the Fourier transforms (denoted by $\sim$) of the ideal global MR-signal $S_0(k_x, k_y)$ and transfer functions $H_{x_0y_0}(k_x, k_y)$ which corresponds to the convolution of the ideal imaged object $\rho_0(x, y)$ and the point-spread-functions:

$$\begin{aligned}\rho(x, y) &= \tilde{S}_0(k_x, k_y) \otimes \tilde{H}_{x_0y_0}(k_x, k_y)\\ &= \rho_0(x, y) \otimes PSF_{x_0y_0}(x, y)\end{aligned} \quad (3)$$

The *PSF* describes the mapping of a delta peak (with properties contained in the transfer function) located at (x_0, y_0) into object space. A more detailed version of the theory and properties of the point-spread-functions used for our purposes can be found in the appendix of this paper.

While the velocities during the very short switching times of the bipolar gradients (of the order of a few ms) can be approximated to be constant the situation changes, however, if (as with k-space segmentation) several phase encoding steps are acquired within a single time frame of the CINE series. Since data is sampled over several acquisition cycles (e.g. ECG cycles) changes in velocities from one k-space line to another will result in different velocity induced first order signal phases $\Delta\phi_1(v_k)$, which vary stepwise along the phase encoding direction (k_y) for block wise segmented acquisition (Fig. 2).

Thus simulations of the resulting values in the velocity encoded phase images can be limited to one-dimensional calculations along k_y and y. In first order approximation phase contrast examinations result in an additional signal phase $\Delta\phi_1(k_y, v_k(\vec{r}))$ in local MR signal components, which depends on the k-space position along the phase encoding direction (k_y).

$$S_{x_0y_0}(\vec{k}) = S_{0,x_0y_0}(\vec{k})e^{-i\Delta\phi_1(k_y,v_k(\vec{r}_0))} \quad (4)$$

The properties of mapping of the velocities into object space can be simulated by calculation the PSF for a delta shaped object. The additional phase factor in equation (4) corresponds to the transfer function $H_{\Delta\phi}(k_y)$ by which the ideal signal is modified due to velocity induced first order phase shifts.

$$H_{\Delta\phi,x_0y_0}(k_x, k_y) = e^{-i\Delta\phi_1(k_y,v_k(\vec{r}_0))} \quad (5)$$

Using equation (3) the resulting complex MR images $\rho(x, y)$ can now be simulated by convolution of the *PSF* with an ideal object. In this case the transfer function $H(k_y)$ corresponds to a product of the sampling function $H_S(k_y)$ (discrete and finite sampling) and an additional $H_{\Delta\phi}(k_y)$ which describes the velocity induced signal phases along k_y:

$$H(k_y) = H_S(k_y)\, H_{\Delta\phi}(k_y) \tag{6}$$

Here global transfer functions are used, which imply homogenous and spatially independent object properties, i.e. identical proton densities and velocity profiles for all pixels of the simulated object. The sampling transfer function can always considered to be global since the same sampling strategy applies to all local signal components. For this kind of simulations it is thus sufficient to calculate the *PSF* for any arbitrary spatial location and to use this global *PSF* for the simulation process.

A more detailed description of the sampling transfer function $H_S(k_y)$ for standard Fourier data acquisition is given in the appendix.

3. Materials and methods

3.1. Simulations

All calculations were performed using one-dimensional transfer- and point spread functions along k_y and y respectively. Global point-spread-functions representing different velocity profiles for homogenous object motion of an ideal rectangular object were calculated for $x_0 = y_0 = 0$. Convolution according to equation (3) corresponds to the mapping of an ideal object with constant proton density and rigid body motion into object space.

All calculations were performed on a standard personal computer using code written in MATLAB (The Math Works Inc., Natick, USA).

3.2. Phantom measurements

All phantom measurements were performed on a 1.5T scanner (Sonata, Siemens, Germany). The pulse sequences for data acquisition consisted of a k-space segmented gradient echo sequences with (temporal resolution = 64 ms) and without (temporal resolution = 104 ms) view sharing but otherwise identical parameters (TE = 5 ms, TR = 6 ms, $\alpha = 15°$, slice thickness = 8 mm, 300 × 400 mm^2 rectangular FOV). 16 phase encoding steps per CINE time frame were sampled within each acquisition cycle. Velocity encoding was performed by adding a bipolar gradient (v_{enc} = 20 cm/s) after each rf-pulse to the otherwise identical pulse sequences.

To reconstruct each phase of the cardiac cycle a full k-space data set is required. In the case of view sharing, however, certain outer regions of k-space are not directly sampled with the corresponding time frame. Thus, for image reconstruction, the full data matrices have to be generated by filling in signals from earlier and later cardiac phases. In case of two fold sampling of the center of k-space compared to outer sections data from these areas are shared by neighboring frames. Even with this simple sampling scheme the duration corresponding to one frame of a given k-space segmented pulse sequence can be significantly reduced. The improvement in temporal resolution depends on the size of the sections in k-space with higher sampling frequencies. In Fig. 3 an example for the distribution of data in k-space as a function of CINE time frames (e.g. cardiac phases) within one acquisition cycle is given. The sampling scheme is periodically repeated over a number of successions (e.g. ECG cycles) until the raw data matrices are completely filled and the desired spatial resolution is reached.

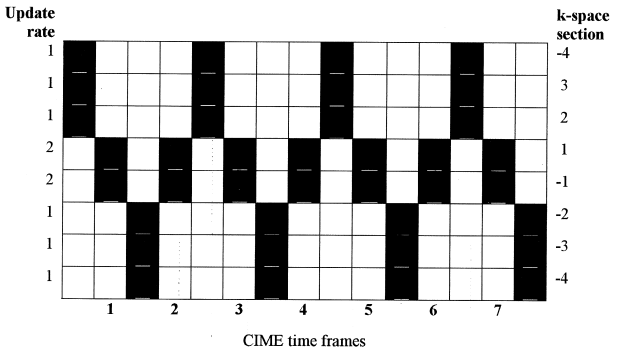

Fig. 3. k-space sampling scheme for 7 CINE time frames for a sampling rate of 2 for the central region of k-space. Images for each cardiac phase are reconstructed using data of the central part and from the 2 neighboring outer sections.

View sharing was implemented with a doubled update rate of the central part of k-space corresponding to ¼ of the whole data set. Based on the approach for a k-space segmented phase contrast gradient echo sequence with 16 phase encoding steps for each frame of the cardiac cycle a temporal resolution of 64 ms could be achieved. In case of this two fold sampling of the center of k-space compared to outer sections data from these areas are shared by neighboring frames.

For all phase contrast measurements an oscillation phantom was build, which could be used to generate a sine shaped velocity profile for a homogenous rectangular object. Measurements could be triggered to the maximum elongation of the oscillation phantom in order to acquire the data over several oscillation cycles analogous to ECG gating in cardiovascular applications of phase contrast measurements.

4. Results

4.1. Simulations

The results of the simulated mapping of the object are displayed in Fig. 4, which shows exemplary results for

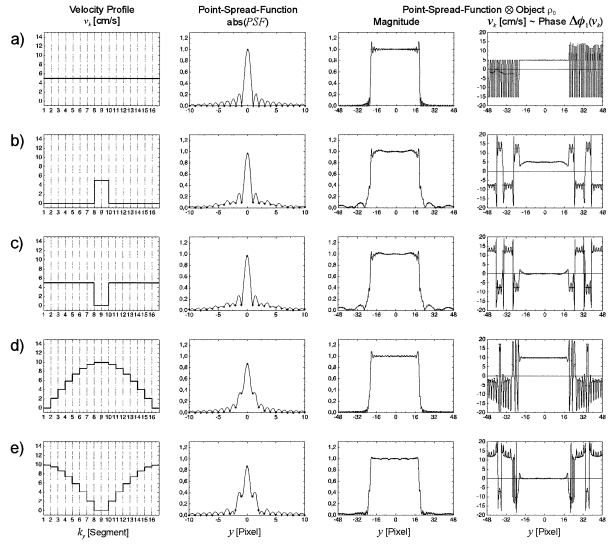

Fig. 4. One-dimensional point spread functions (absolute values) as well as magnitude and phase of the simulated object for different velocity profiles (a–g) along k_y. All *PSF*s were calculated for $x_0 = y_0 = 0$. Convolution with a rectangular object permits the simulation of magnitude and phase in the reconstructed MR image for a homogenous rectangular object with a spatial extension of 40 pixels and identical motion of all object pixels corresponding to the respective velocity profile. The data points represent the pixel intensities in the reconstructed MR image while the solid lines correspond to a 10-fold higher spatial resolution of the *PSF*. The pixel intensities in the phase images are converted into encoded velocities (equation (1)).

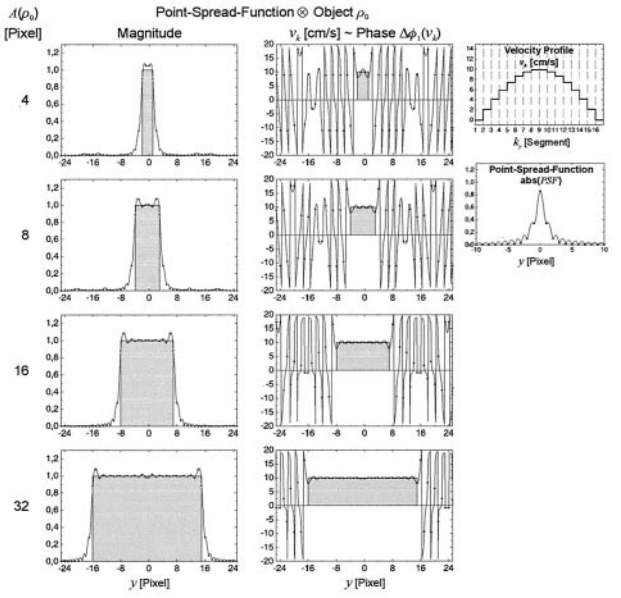

Fig. 5. Magnitude and phase in the simulated MR image for homogenous rectangular objects with different spatial extensions. Velocity profile and point spread function are identical for all object sizes. The data points represent the pixel intensities in the reconstructed MR image while the solid lines correspond to a 10-fold higher spatial resolution. The pixel intensities in the phase images are already converted into encoded velocities.

different motion patterns based on k-space segmented data acquisition with 16 k-space segments. The results demonstrate that the velocities, which reflect flow or motion during acquisition of the central k-space regions clearly dominate the encoded velocities in the reconstructed phase images whereas magnitude images show only minor modifications for all velocity profiles.

Due to discrete and finite sampling (equation A7–A9) the outcome of the simulations are sinc-like *PSF*s, which are modulated by the different time courses of the signal phase. Constant object velocities over the whole CINE time frame (a) lead, as expected, to a constant signal phase and thus an ideal mapping of the velocities into the reconstructed phase image, which demonstrates homogenous pixel intensities (data points) along the rectangular object in the magnitude as well as phase image.

The additional simulations (b–e) immediately show that the underlying object motion, which is represented by the object velocities during acquisition of the central part of k-space, mainly determines the values in the phase images and thus the measured velocities. This is particularly evident for the examples b and c. Here, identical but temporally shifted velocity profiles are chosen in such a way that in one case maximum object velocities are situated in the center of k-space whereas velocities vanish for the remaining raw data (b) and vise versa (c).

For velocities sampled in the central k-space regions the mapping into object space is almost undisturbed even for flow or motion occurring during the acquisition of only ⅛ of the raw data matrix (b). For identical velocities located at or near the borders of k-space (c), however, pixel intensities in the phase images are close to zero and therefore again match with the object motion during acquisition of the center of k-space. Similar results are obtained for simulations shown in Fig. 4d and 4e, which display more realistic examples of velocity profiles if compared to characteristic cyclic blood flow or tissue motion patterns. In addition the filtering effect determined by the position of the central k-space part relative to the flow or motion pattern Fig. 4 also demonstrates that non-constant velocities result in artifacts in magnitude and phase images, which are visible as signal modulations located mainly at and near the edges of the simulated object.

Central parts, on the other hand, show homogenous intensities. Therefore not only the shape of the velocity profile but also the spatial extension of the moving object and thus the influence of the edge intensities have to be considered in order to analyze the properties of the phase images and encoded velocities. Since in clinical applications of phase contrast measurements regional different flow or motion patterns have to resolved the role of these properties is highly relevant for the reliability of the quantified velocities. For that reason additional simulations including different spatial extensions of rectangular objects were carried out. The results for a sine shaped velocity profile and four different object sizes are given in Fig. 5. The gray shaded areas correspond to the ideal rectangular object used for the

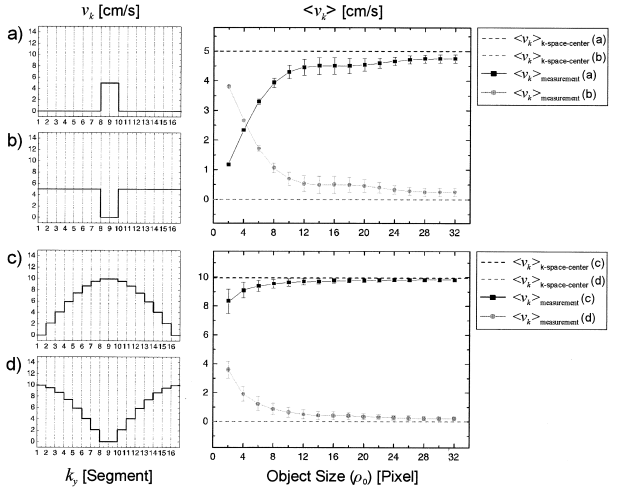

Fig. 6. Averaged simulated object velocities $\langle v_k \rangle$ as a function of spatial extension of a rectangular object for four different velocity profiles. The dashed lines indicate the mean velocities at the time of acquisition of the central part of k-space (2 out of 16 k-space segments, i.e. 1/8 of the total raw data matrix).

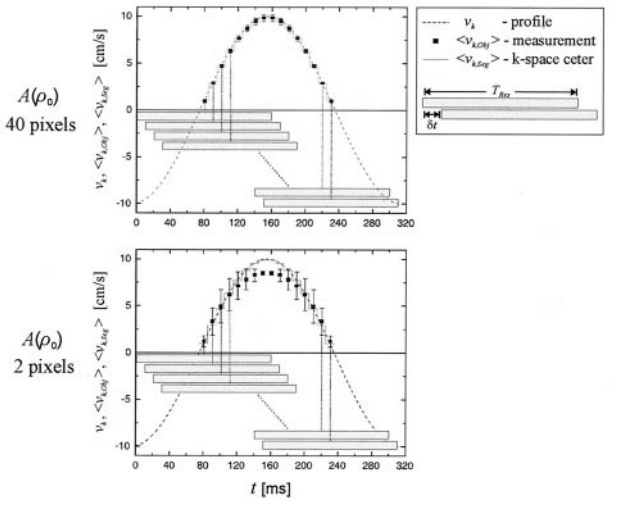

Fig. 7. Simulated phase contrast measurement for a sine shaped velocity profile and successive shifting of a CINE time frame. The temporal resolution T_{Res} was chosen to be one half of the cyclic flow or motion pattern. The dashed line represents the underlying velocity profile $v_k(t)$. Mean velocities $\langle v_{k,Seg} \rangle$ at the time of acquisition of the central part of k-space (2 out of 16 k-space segments, i.e. 1/8 of the total raw data matrix) are indicated by the step function (solid gray line). Single data points correspond the mean encoded (measured) object velocities $\langle v_{k,Obj} \rangle$ based on point-spread-functions calculated for CINE time frames, which were shifted one after the other by δt with respect to the velocity profile.

simulations. The object height in the phase images (converted into encoded velocities v_k) was chosen as the magnitude of the velocities in the central 1/8 of k-space.

For all object sizes the data acquired in the center of k-space dominate the resulting values in the phase images. However, disturbed signal intensities at the edges play a greater role for smaller object sizes and thus influence the encoded velocities to a greater degree if compared to larger objects.

In order to assess the influence of object size in a more quantitative manner the encoded velocities were simulated for increasing object sizes in 2 pixel steps and averaged over the respective object's extension. The results for four different velocity profiles were plotted as a function of object size and demonstrate the relationship between the potential to detect peak velocities with respect to the size of the moving object as well as the position of the center of k-space relative to the velocity profile (Fig. 6).

For all simulations the mean object velocities approach the values representing the central k-space velocities (dashed horizontal lines) for increasing object size. The simulations concerning instructive but unrealistic motion patterns a) and b) demonstrate the dominant role of central k-space regions starting from object sizes larger than 10–12 pixels. For more realistic velocity profiles c) and d) it can be seen that even for small object sizes of 2–4 pixels the encoded velocities are of the order of 80% determined by the mid k-space section. Velocities for larger objects are almost exclusively encoded by the induced phase shifts located in the center of k-space.

For that reason the dynamics of an underlying cyclic motion can even be resolved using a phase contrast pulse sequence with insufficient temporal resolution if several measurements are performed and the single CINE time frames are successively shifted with respect to the velocity profile. Fig. 7 shows the results of simulations based on a sine shaped velocity profile and a CINE time frame with a duration of one half of the period of the motion pattern. In order to take into account the influence of the edge intensities calculations were performed for two largely different object sizes of 2 and 40 pixels respectively.

The agreement of the simulated data points with the velocity profile is clearly visible. Although the length of the time frame is chosen by far too large to resolve the motion pattern within a single measurement successive shifting of the acquisition window and thus the center of k-space permits the assessment of the object dynamics with high accuracy. Even for an object size of 2 pixels the temporal evolution of the velocities can still be determined while peak velocities are underestimated by a factor of approximately 20%. In this case the phase contrast measurement leads to a low pass filtered velocity profile, which, however, still allows the assessment of the principal motional dynamics.

Since all above simulation results indicate that velocities measured by phase contrast MRI are to a high degree encoded within the central part of k-space frequent acquisition of those regions provides a suitable and useful method to significantly improve the detection of the dynamics of the underlying flow or motion patterns. One possibility to achieve an increased sampling rate of central k-space regions is thus the use of view sharing techniques for data acquisition.

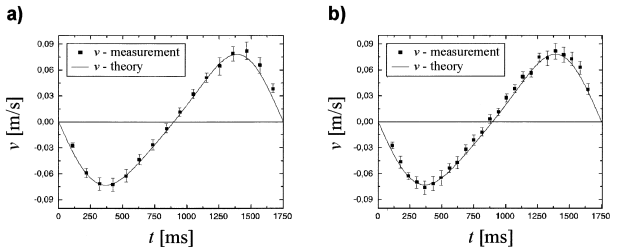

Fig. 8. Mean measured velocities for one oscillation period as a function of time t after the trigger pulse for pulse sequences with (b) and without (a) view sharing. The solid line represents expected velocities. The position of the data points with respect to time t corresponds to the acquisition of the central k-space line.

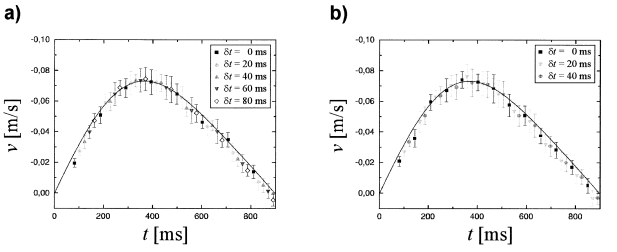

Fig. 9. Temporally shifted CINE series of mean measured velocities for the first half of the phantom's oscillation period for pulse sequences with (b) and without (a) view sharing. The solid line represents the theoretical velocities as a function of time after the trigger signal ($t = 0$ ms). Averaged object velocities resulting from measurements with step-wise increased temporal shifts δt with respect to the trigger impulse are displayed as different data points. For measurements with view sharing (b) two additional temporally shifted CINE acquisitions are sufficient until the time frames again match those of the standard acquisition ($\delta t = 0$ ms) while without view sharing 4 additional measurements are necessary.

4.2. Phantom measurements

In comparison to a standard k-space segmented gradient echo sequence the application of view sharing results in a clear increase of temporal resolution. If our view sharing implementation is directly compared to a pulse sequence with identical parameters using standard reconstruction the gain in acquisition speed is 37.5%.

In order to compare measured and theoretical values the velocity components for each CINE time frame were averaged over the phantom and plotted against time t. Fig. 8 shows the results of phantom measurements with (b) and without (a) view sharing. The results demonstrate high consistency of the measured and theoretical velocities for both acquisition modalities. In addition it is clearly visible that the application of view sharing improves the time resolved detection of the dynamics of the underlying flow or motion pattern without loss of functional information. More frequent sampling of central parts of k-space results in increased functional information in good agreement with the theoretical considerations on the basis of the point spread function simulations. Thus view sharing techniques clearly improve detection and representation of fast changes in blood flow patterns or tissue motion.

In order to validate the simulation results concerning the role of the different k-space regions measurements can be performed analogous to the calculations represented in Fig. 7 by successively shifting the CINE time frames with respect to the trigger impulse, which marks the beginning of each oscillation period. For that consecutive measurements with acquisition windows respectively shifted by $\delta t = 20$ ms were performed. The resulting CINE series of encoded velocities correspond to different positioning of the central k-space regions with respect to the velocity profile of the oscillating phantom.

Fig. 9 depicts the results of such measurements and clearly demonstrates that the phantom velocities correspond well with the theoretical values and can be assessed with high accuracy by temporally shifting of the CINE time frames. Despite the insufficient length of the singe CINE time frames (64 ms and 104 ms) for a detection of the velocity profile with a temporal resolution of 20 ms this can be achieved by temporally shifting according to Fig. 7 since the underlying velocities are to a major part encoded within the central k-space regions. These results are in good agreement with the outcome of the point-spread-function based simulations.

5. Discussion

View Sharing in combination with k-space segmented phase contrast MRI has proven to be a suitable method for improvement of temporal and/or spatial resolution in velocity mapping applications. Due to the k-space weighted properties of velocity mapping demonstrated by simulations based on point-spread-function calculations it could be shown that view sharing is applicable to phase contrast methods if appropriate k-space sampling schemes are chosen. Acquisition of the k-space center with respect to the velocity profile primarily determines the resulting values measured with phase contrast MRI.

In further simulations with different object sizes it could also be verified that even for small regions of the order of 2–4 pixels the peak velocities and dynamics of the flow or motion patterns can still be resolved with an accuracy of approximately 80% if compared to peak velocities. For larger object sizes phase contrast imaging with view sharing permits the assessment of the dynamics with considerably higher temporal resolution and almost no loss of functional information in comparison to standard k-space segmented methods.

These properties of the view sharing techniques could be verified by measurements with an oscillating phantom using k-space segmented gradient echo pulse sequences with and without view sharing. The results exhibit a high consistency of the measured and theoretical velocities, which are known from the geometry of the phantom. In addition an excellent agreement with the theoretical simulations could be found

and the potential of view sharing to improve the detection of flow or motion patterns could be demonstrated.

Regarding temporal resolution of the CINE images and magnitude of the underlying object velocities the simulations and phantom measurements discussed in this paper are mainly focused on cardiac applications. For velocity profiles with higher peak velocities and faster varying pulsatile motion patterns as in blood flow waveforms the temporal resolution of the pulse sequences has to be adjusted by more frequent updates of central k-space lines and thus fewer k-space segments and overall shorter CINE time frames.

If appropriate temporal resolution, venc factor and sampling scheme are chosen according to the respective motion patterns k-space segmented phase contrast MRI with view sharing permits significant increase in temporal and/or spatial resolution due to the properties of velocity mapping associated with the k-space position and provides an efficient way to increase function information within the same total acquisition time.

The improvement of the temporal resolution within the ECG-cycle with view sharing is highly relevant for the observation of blood flow or tissue motion dynamics during the systolic phase in humans.

Appendix

Theory, Point-Spread-Function

Point-spread-functions in combination with idealized objects can be used to analyze the properties of mapping of MR images into object space. The relation between the measured signal $S(k_x, k_y)$ and the reconstructed complex MR image $\rho(x, y)$ is given by the pair of Fourier transforms:

$$S(k_x, k_y) = \hat{\rho} = \int_{x'}\int_{y'} \rho(x, y)e^{ik_x x}e^{ik_y y}\mathrm{d}x\mathrm{d}y,$$
$$\rho(x, y) = \tilde{S} = \int_{k_{x'}}\int_{k_{y'}} S(k_x, k_y)e^{-ik_x x}e^{-ik_y y}\mathrm{d}k_x\mathrm{d}k_y. \quad \text{(A1)}$$

The local signal components $S_{xy}(k_x, k_y)$ measured in an MR experiment can be written as a product of the ideal MR signal $S_{0,xy}(k_x, k_y)$ and a spatially dependent transfer function $H_{xy}(k_x, k_y)$, which describes the locally different influences on the ideal MR signal.

$$S_{xy}(k_x, k_y) = S_{0,xy}(k_x, k_y)\, H_{xy}(k_x, k_y) \quad \text{(A2)}$$

Integration over the total measured object leads to the detected MR signal $S(k_x, k_y)$, which is related to the pixel intensities in object space by the Fourier transform (equation A1). Using the connection between ideal MR signal S_0 and proton density $\rho_0(x, y)$ the ideal local signal component at the spatial location (x_0, y_0) is given as

$$S_{0,x_0y_0}(k_x, k_y) = \int_{x'}\int_{y'} \rho_0(x, y)\delta(x - x_0)\delta(y - y_0)e^{ik_x x}e^{ik_y y}\mathrm{d}x\mathrm{d}y$$
$$= \rho_0(x_0, y_0)e^{ik_x x_0}e^{ik_y y_0}. \quad \text{(A3)}$$

Combination with equation (A2), integration over the total measured object, inserting into equation (A1) and interchanging of integration variables results in an equation connection the ideal proton density and the point spread function (*PSF*).

$$\rho(x, y) = \tilde{S} = \int_x\int_y \rho_0(x_0, y_0) \underbrace{\left(\int_{k_{x'}}\int_{k_{y'}} H_{x_0y_0}(k_x, k_y)e^{-ik_x(x-x_0)}e^{-ik_y(y-y_0)}\right)}_{PSF_{x_0y_0}} \mathrm{d}x_0\mathrm{d}y_0 \quad \text{(A4)}$$

The expected complex MR-image $\rho(x, y)$ can thus be calculated by convolution of the Fourier transforms (denoted by $\sim$) of the ideal MR-signal S_0 and a transfer function H which corresponds to the convolution of the ideal imaged object $\rho_0(x, y)$ and the point-spread-function which is defined as the Fourier transform of the corresponding transfer function. In short notation ($\otimes$ = convolution) equation (A4) can be written as

$$\rho(x, y) = \tilde{S}_0(k_x, k_y) \otimes \tilde{H}_{x_0y_0}(k_x, k_y)$$
$$= \rho_0(x, y) \otimes PSF_{x_0y_0}(x, y) \quad \text{(A5)}$$

In the simplest case with an ideal delta shaped object $\rho_0(x, y) = \delta(x - x_0)\delta(y - y_0)$ located at (x_0, y_0) the MR image directly corresponds to the Fourier transform of the transfer function. Thus the complex pixel intensities in object space are determined by the point spread function originating from (x_0, y_0):

$$\rho(x, y) = PSF_{x_0y_0}(x, y) = \int_{k_{x'}}\int_{k_{y'}} H_{x_0y_0} \cdot (k_x, k_y)e^{-ik_x(x-x_0)}e^{-ik_y(y-y_0)}\mathrm{d}k_x\mathrm{d}k_y \quad \text{(A6)}$$

For a homogenous measured object with identical and spatial independent object properties the transfer function can be considered as a global function H. It is thus sufficient to calculate the *PSF* for an arbitrary spatial location inside the object and calculate the expected pixel intensities by convolution the *PSF* with the ideal proton density $\rho_0(x, y)$. These considerations are also valid for data acquisition or reconstruction methods (e.g. finite and discrete sampling, zero filling etc.), which are independent of local object specific properties.

According to equation (A4) locally varying motion pat-

terns (which are not considered here), on the other hand, require the use of pixel wise different point-spread-functions. In that case the calculation of complex MR images $\rho(x, y)$ the convolution of a simulated object has to be carried out using a set of spatially dependent *PSF*s, which describe locally different signal properties (equation A4).

The sampling function for typical Fourier encoding is given by a finite set of delta functions equidistantly located on a two-dimensional regular grid.

$$H_S(k_x, k_y) = \sum_{l=1}^{N_x} \sum_{m=1}^{N_y} \delta(k_x - k_{lx})\delta(k_y - k_{my}), \quad \text{(A7)}$$

$$\text{with} \quad k_{lx} = -k_{x,\max} + (l-1)\Delta k_x \quad \text{and}$$

$$k_{my} = -k_{y,\max} + (m-1)\Delta k_y. \quad \text{(A8)}$$

For $N_x N_y$ acquired data points the sampling intervals are defined by Δk_x and Δk_y respectively. Inserting equation (A7) into (A6) results in a *PSF* for $x_0 = y_0 = 0$:

$$PSF(x, y) = \sum_{l=1}^{N_x} \sum_{m=1}^{N_y} e^{-ik_{lx}x} e^{-ik_{my}y}. \quad \text{(A9)}$$

References

[1] McVeigh ER. MRI of myocardial function: motion tracking techniques. Magn Reson Imaging 1996;14:137–50.

[2] Dumoulin CL. Phase contrast MR angiography techniques. Magn Reson Imaging Clin N Am 1995;3:399–411.

[3] Walker MF, Souza SP, Dumoulin CL. Quantitative flow measurement in phase contrast MR angiography. J Comput Assist Tomogr 1988; 12:304–13.

[4] Firmin DN, Nayler GL, Klipstein RH, Underwood SR, Rees RS, Longmore DB. In vivo validation of MR velocity imaging. J Comput Assist Tomogr 1987;11:751–6.

[5] Firmin DN, Nayler GL, Kilner PJ, Longmore DB. The application of phase shifts in NMR for flow measurement. Magn Reson Med 1990; 14:230–41.

[6] Underwood SR, Firmin DN, Rees RS, Longmore DB. Magnetic resonance velocity mapping. Clin Phys Physiol Meas 1990;11:37–43.

[7] Haacke EM, Li D, Kaushikkar S. Cardiac MR imaging: principles and techniques. Top Magn Reson Imaging 1995;7:200–17.

[8] Pelc NJ, Herfkens RJ, Shimakawa A, Enzmann DR. Phase contrast cine magnetic resonance imaging. Magn Reson Q 1991;7:229–54.

[9] Pelc LR, Sayre J, Yun K, Castro LJ, Herfkens RJ, Miller DC, Pelc NJ. Evaluation of myocardial motion tracking with cine-phase contrast magnetic resonance imaging. Invest Radiol 1994;29:1038–42.

[10] Drangova M, Zhu Y, Bowman B, Pelc NJ. In vitro verification of myocardial motion tracking from phase-contrast velocity data. Magn Reson Imaging 1998;16:863–70.

[11] Hennig J, Schneider B, Peschl S, Markl M, Krause T, Laubenberger J. Analysis of myocardial motion based on velocity measurements with a black blood prepared segmented gradient-echo sequence: methodology and applications to normal volunteers and patients. J Magn Reson Imaging 1998;8:868–77.

[12] Markl M, Schneider B, Hennig J, Peschl S, Winterer J, Krause T, Laubenberger J. Cardiac phase contrast gradient echo MRI: measurement of myocardial wall motion in healthy volunteers and patients. Int J Card Imaging 1999;15:441–52.

[13] Lee VS, Spritzer CE, Carroll BA, Pool LG, Bernstein MA, Heinle SK, MacFall JR. Flow quantification using fast cine phase-contrast MR imaging, conventional cine phase-contrast MR imaging, and Doppler sonography: in vitro and in vivo validation. AJR Am J Roentgenol 1997;169:1125–31.

[14] Mohiaddin RH, Pennell DJ. MR blood flow measurement. Clinical application in the heart and circulation. Cardiol Clin 1998;16:161–87.

[15] Nayler GL, Firmin DN, Longmore DB. Blood flow imaging by cine magnetic resonance. J Comput Assist Tomogr 1986;10:715–22.

[16] Thomsen C, Cortsen M, Sondergaard L, Henriksen O, Stahlberg F. A segmented K-space velocity mapping protocol for quantification of renal artery blood flow during breath-holding. J Magn Reson Imaging 1995;5:393–401.

[17] Kozerke S, Scheidegger MB, Pedersen EM, Boesiger P. Heart motion adapted cine phase-contrast flow measurements through the aortic valve. Magn Reson Med 1999;42:970–8.

[18] Schulen V, Schick F, Loichat J, Helber U, Huppert PE, Laub G, Claussen CD. Evaluation of K-space segmented cine sequences for fast functional cardiac imaging. Invest Radiol 1996;31:512–22.

[19] Arai AE, Gaither CC, Epstein FH, Balaban RS, Wolff SD. Myocardial velocity gradient imaging by phase contrast MRI with application to regional function in myocardial ischemia. Magn Reson Med 1999; 42:98–109.

[20] Grist TM, Polzin JA, Bianco JA, Foo TK, Bernstein MA, Mistretta CM. Measurement of coronary blood flow and flow reserve using magnetic resonance imaging. Cardiology 1997;88:80–9.

[21] Hennig J. K-space sampling strategies. Eur Radiol 1999;9:1020–31.

[22] Doyle M, Walsh EG, Blackwell GG, Pohost GM. Block regional interpolation scheme for k-space (BRISK): a rapid cardiac imaging technique. Magn Reson Med 1995;33:163–70.

[23] Doyle M, Walsh EG, Foster RE, Pohost GM. Rapid cardiac imaging with turbo BRISK. Magn Reson Med 1997;37:410–7.

[24] Foo TK, Bernstein MA, Aisen AM, Hernandez RJ, Collick BD, Bernstein T. Improved ejection fraction and flow velocity estimates with use of view sharing and uniform repetition time excitation with fast cardiac techniques. Radiology 1995;195:471–8.

[25] Polzin JA, Frayne R, Grist TM, Mistretta CA. Frequency response of multi-phase segmented k-space phase-contrast. Magn Reson Med 1996;35:755–62.

[26] Jones RA, Haraldseth O, Muller TB, Rinck PA, Oksendal AN. K-space substitution: a novel dynamic imaging technique. Magn Reson Med 1993;29:830–4.

[27] Parrish TB, Hu X. Hybrid technique for dynamic imaging. Magn Reson Med 2000;44:51–5.

[28] Rossmann K. Point Spread-Function, Line Spread-Function and Modulation Transfer Function: Tools for the Study of Imaging Systems. Radiology 1969;14:257–72.

[29] Haacke M, Brown R, Thompson M, Venkatesan R. Magnetic Resonance Imaging. New York: Wiley-Liss; 1999.